ENHANCEMENT OF DYNAMIC VOLTAGE RESPONSE IN UPF MODE OF DFIG WIND TURBINE DURING GRID DISTURBANCES USING STATCOM AND SAPF

Mohamed A. Ali[1], Hazem Hassan Ali[2]

[1]Faculty of Engineering Shoubra, Benha University, Cairo, Egypt
[2]College of Industry and Energy Technology, New Cairo Technological University, Cairo, Egypt,
hazemhassan481@yahoo.com

Abstract *- Protection of Doubly Fed Induction Generator (DFIG) wind turbine from failure operation due to grid disturbances is necessary via accomplishing reactive power compensation. Static Synchronous Shunt Compensator (STATCOM) based on AC voltage magnitude regulator and Shunt Active Power Filter (SAPF) based on load calculations at Point of Common Coupling (PCC) are used to enhance the dynamic response of DFIG regulated voltage during grid disturbances. An assessment performance study between these devices is introduced in this paper. STATCOM and SAPF are proposed under the presence of the weak grid and the power converter of DFIG is operated in Unity Power Factor (UPF) mode. Also, the maximum energy production of DFIG using Genetic Algorithm (GA) optimization feeding the load and the grid is still working over the entire operation. Simulation results reveal that STATCOM enhanced the dynamic voltage response of DFIG compared to SAPF under grid disturbances and wind speed variation.*

Keywords: *DFIG wind turbine; MPPT; STATCOM; Shunt active power filter; PI controller; Power quality; Voltage terminal regulation.*

1. Introduction

Most of Doubly Fed Induction Generator (DFIG) large size wind turbines based Wind Energy Conversion System (WECS) are in isolated places due to its noise pollution. Those areas have weak electric power grids with low fault current ratios, low reactance/resistance ratio of the transmission line and under voltage conditions. Conventional reactive power compensation devices especially in weak grid interconnected with DFIG wind turbines like AC filters cannot adjust reactive power balance continuously [1]. This paper presents Static Synchronous Shunt Compensator (STATCOM) and Shunt Active Power Filter (SAPF) based different reactive power control strategies to realise continuous adjustment. DFIG wind turbine is designed to do its function and track the maximum power between cut-in speed and rated wind speed under grid disturbances and different wind speed. The peak power is obtained by speed regulator in Rotor Side Converter (RSC) of DFIG which regulates the rotor speed at optimum value using Genetic Algorithm (GA) optimization via optimum Tip Speed Ratio (TSR) technique that achieves the peak power coefficient [2]-[3].

There are problems produced from grid disturbances happened in weak grid interconnected with DFIG wind turbines such as loss of speed, influence on the performance of generator, and peak current due to voltage sag occurrence and damage of insulation of generator due to voltage swell occurrence. Where the grid disturbances used here in this study are sudden inductive load, sudden capacitive load, and three phase fault.

The right observing of voltage stability response versus real-time in a power system under grid disturbances and wind speed variation is needed for protecting generator and working efficiently at any condition. The bus voltage at Point of Common Coupling (PCC) is local quantity so it is very costly to control the bus voltage at the remote node by the use of conventional power stations. It is because the reactive power flow in the system is related to changes in voltage which increases the power losses in the electric grid. Hence, it is important to install voltage control devices in the transmission or distribution network even if the wind turbine has voltage controlling capability because the wind turbines are located at a far distance location from the load center [4].

To overcome this problem, one of Flexible AC Transmission Systems (FACTS) devices based power electronic converters such as STATCOM is used and one of active power filter devices like SAPF is also used. The two devices each separately are used to regulate the terminal voltage of DFIG at its nominal level. Where, STATCOM based AC voltage magnitude regulator and SAPF based load calculations are tested by connecting each of them separately in parallel with the sudden load at PCC. The sudden load is connected to PCC through three phase circuit breaker. The sudden load in the first case is inductive load causes a disturbance leads to voltage sag and in the second case is a capacitive load causes a

disturbance leads to voltage swell. Also, STATCOM and SAPF each separately are tested under three phase fault as a grid disturbance happened through using ground resistance. The cases under study represent the grid power quality disturbances. The selection of these study cases is according to the power quality indices mentioned in different international standards and specifications such as IEC 62271-100 for high voltage switchgear limits, IEC 60255 for medium voltage limits, and IEC 364 for low voltage installation [5-6]. MATLAB /Simulink environment is used to implement the cases under study. The results of the simulations for previous mentioned cases are examined, with and without compensation, to indicate the advantages and differences between performance of STATCOM and SAPF design for power quality improvement and voltage regulation of DFIG wind turbine.

This study is arranged as follows. Section 2 summarizes the related work. The wind turbine description is elaborated in Section 3 to find out the aerodynamic system and the operating regions of wind turbine. In Section 4, it describes the TSR optimum technique using GA optimization. In Section 5, it indicates the way of solving power coefficient equation in terms of pitch angle and TSR using GA. The fourth order state-space model of the DFIG wind turbine is described in Section 6. A design of the RSC control circuit based speed regulator and Grid Side Converter (GSC) based DC-link voltage regulator are explained in Section 7 to illustrate how DFIG tracks the maximum power point and keeps the DC-link voltage at a constant required level for RSC. Operating DFIG wind turbine before occurrence of grid disturbances is demonstrated in Section 8. Appearance of grid disturbances effect before using STATCOM and SAPF is explained in Section 9. In section 10, it illustrates the design of STATCOM. In section 11, it explains the control scheme of SAPF. In section 12, the PI controller method used for all regulators in this study is demonstrated with values. Moreover, the digital simulation results are discussed in Section 13 under wind speed variation followed by a conclusion in Section 14.

2. Related work

Significant research on the dynamic voltage response of DFIG wind turbine has been reported in the literature with Stability Improvement of DFIG-Based Wind Farm Integrated Power System Using ANFIS Controlled STATCOM [7] included how to achieve system stability using STATCOM based on intelligence technique but the performance between STATCOM and SAPF based on voltage control has not been illustrated. Static Reactive Power Compensator Design, Based on Three-Phase Voltage Converter [8] mainly introduced only how to design STATCOM based on three phase voltage converter in regulating of terminal voltage using conventional controllers for renewable energy and its role in achieving fast response compared to SVC, but the effect of voltage sag and swell were not studied. A Simulation Model for Providing Analysis of Wind Farms Frequency and Voltage Regulation Services in an Electrical Power System [9] only considered accomplishing of the voltage regulation via power converter of the wind turbine under load condition, but the comparative analysis study between STATCOM and SAPF under effect of voltage sag and swell are not studied .While some researchers have concentrated on the Power Quality Issues and Mitigation for Electric Grids with Wind Power Penetration [10], it was only concluded that the voltage fluctuations due to wind intermittency based on Saudi daily load profile can be mitigated via reactive power compensation of the interface inverter without any illustration to control schemes of these devices. MPPT operation can be accomplished using traditional methods without using current control based on intelligence techniques for MPPT performance. The paper Maximum power production operation of doubly fed induction generator wind turbine using adaptive neural network and conventional controllers [11] focused only how to track the maximum power point using conventional and intelligence techniques, but the voltage regulation effect under this operation is not considered. The paper Two-Level Grid-Side Converter-Based STATCOM and Shunt Active Power Filter of Variable-Speed DFIG Wind Turbine-Based WECS Using SVM for Terminal Voltage [12] proposed only a voltage regulation of DFIG wind turbine via modification of GSC control circuit to operate as SAPF and STATCOM separately, but the fault occurrence is not studied. In LVRT and Stability Enhancement of Grid-Tied Wind Farm Using DFIG-Based Wind Turbine [13] focused only on accomplishing terminal voltage regulation via control scheme of RSC using conventional regulators by supplying the required amount of reactive power to achieve system stability, but the voltage swell case in not studied.

The main contributions of this study contain on (1) illustration of the performance of STATCOM based AC voltage magnitude regulator and SAPF based load calculations and to illustrate the difference between each performance under different grid disturbances, (2) during the operation of voltage regulation, the power coefficient equation in terms of TSR at zero pitch angle for wind speed less than rated speed is optimized using GA under conditions of the MPPT control region, and (3) a detailed mathematical model for STATCOM to indicate its performance in voltage regulation.

3. Operating region and aerodynamics of the wind turbine

A. Operating region of the wind turbine

The wind turbine works at different dynamics from the cut-in wind speed (4 m/s) to the cut-out wind speed (24 m/s) as illustrated in Figure 1. Three operating wind speed point can be observed in this figure [14]. The important used notations are described in Table 1.

Table 1
Notations

Notation	Description
$P_{m,rated}$	Rated mechanical power (W)
$T_{m,rated}$	Rated mechanical torque (N-m)
V_w	Wind Speed (m/s)
V_{dc}^*	Reference DC-link voltage (V)
C_p	Power coefficient
$C_{p,max}$	Maximum power coefficient
λ	Tip Speed Ratio (TSR)
λ_{opt}	Optimum TSR
β	Pitch angle
ω_t	Rotational turbine speed (rad/s)
$\omega_{t,opt}$	Optimum rotational turbine speed (rad/s)
ω_e	Synchronous angular velocity (rad/s)
ω_r	Rotor electrical angular speed (rad/s)
ω_m	Mechanical angular speed of generator (rad/s)
$\omega_{m,rated}$	Rated value of ω_m (rad/s)
ω_0	Bandwidth frequency (rad/s)
$\omega_{0\omega r}$	Bandwidth frequency of speed regulator (rad/s)
ω_{0Qs}	Bandwidth frequency of var regulator (rad/s)
ω_{0dc}	Bandwidth frequency of DC-link voltage regulator (rad/s)
f_{sw}	Switching frequency (Hz)
ω_{sw}	Switching frequency (rad/s)
ω_{outer}	Bandwidth frequency of outer loop
$v_{s,abc}$	Three phase stator voltages (V)
$i_{s,abc}$	Three phase stator currents (A)
$i_{r,abc}$	Three phase rotor currents (A)
$i_{G,abc}$	Three phase grid currents (A)
$i_{GSC,abc}$	Three phase GSC currents (A)
$i_{DFIG,abc}$	Three phase wind turbine currents (A)
$i_{l,abc}$	Three phase load currents (A)
$i_{f,abc}$	Three phase fault currents (A)
i_{filter}	Three phase filter currents (A)
$v_{stat,d}$	Voltage source converter output voltage in d-axis
$i_{stat,d}$	Converter output current in d-axis
$v_{PCC,d}$	PCC bus voltage in d-axis
$M_{stat,d}$	Modulation index of STATCOM in d-axis
$v_{stat,q}$	Voltage source converter output voltage in q-axis
$i_{stat,q}$	Converter output current in q-axis
$v_{PCC,q}$	PCC bus voltage in q-axis
$M_{stat,q}$	Modulation index of STATCOM in q-axis
C_{dc}	Capacitance of DC-link voltage of STATCOM
v_{PCC}	PCC bus voltage
α_{dc}	Output of DC-link voltage regulator
C_m	Filter capacitor
i_{Gd}	Grid current in d-axis
i_{Gq}	Grid current in q-axis
α_{PCC}	Output of PCC terminal voltage regulator
$i_{stat,d}^*$	Reference converter output current in d-axis
$i_{stat,q}^*$	Reference converter output current in q-axis
$\hat{i}_{Ld}$	Low frequency component of the load current in d-axis
$\hat{i}_{Lq}$	Low frequency component of the load current in q-axis
$\tilde{i}_{Ld}$	High frequency component of the load current in d-axis
$\tilde{i}_{Lq}$	High frequency component of the load current in q-axis
i_0	Load current in zero-axis component
i_{aref}	Compensation reference current in a-axis
i_{bref}	Compensation reference current in b-axis
i_{cref}	Compensation reference current in c-axis

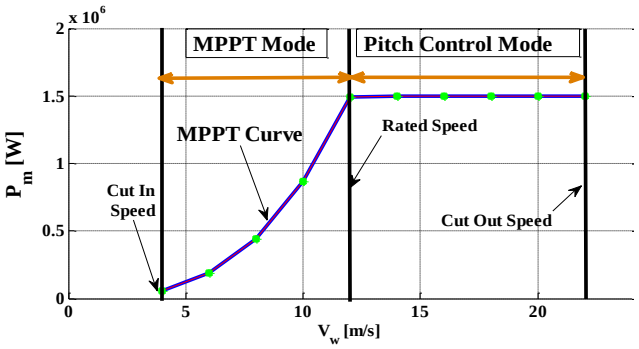

Fig. 1 Power speed curve of variable speed wind turbine.

B. Aerodynamic of the wind turbine

The energy conversion of the wind turbine can be represented by the nonlinear equations as follows [14]:

$$P_m = 0.5\rho A {V_w}^3 C_p \quad (1)$$

Where ρ is the air density (kg/m^3), $A = \pi R^2$ is area covered by turbine blades (m^2), and R is rotor radius (m). The power captured by the wind turbine depends on C_p for a given wind speed. The relationship of $C_p$with λ and β represents output characteristics of the wind turbine as in equation (2):

$$C_p(\lambda,\beta) = 0.5176\left(\frac{116}{\lambda_i} - 0.4\beta - 5\right)e^{-\frac{21}{\lambda_i}} + 0.0068\lambda \quad (2)$$

Where λ is a variable expressing the linear speed of blade tip to speed of wind. λ and $\frac{1}{\lambda_i}$ can be expressed as in equations (3) and (4), respectively.

$$\lambda = \frac{\omega_t R}{V_w} \quad (3)$$

$$\frac{1}{\lambda_i} = \frac{1}{\lambda + 0.08\beta} - \frac{0.035}{\beta^3 + 1} \quad (4)$$

By using equation (2), the typical C_p versus λ curve at various pitch angles β is shown in Figure 2. As mentioned before, there is an optimum value of λ that gives maximum power coefficient $C_{p,max}$. The maximum value of C_p theoretically is nearly 0.59 [14].

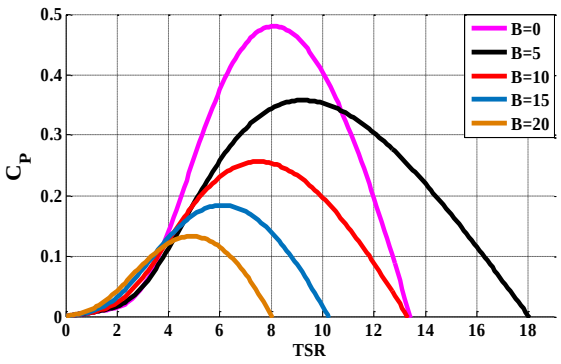

Fig. 2 Power coefficient $C_p(\lambda, \beta)$ versus λ for different values of pitch angle β.

So, in the mode of Maximum Power Point Tracking (MPPT) which is between cut-in wind speed and rated wind speed, If λ is being constant at its optimal value corresponding to $C_{p,max}$, this ensures that the wind turbine is operated at its maximum operating point. Figure 3 shows turbine mechanical power as a function of turbine speed by substituting equations (2), (3) and (4) in equation (1) at various wind speed and TSR λ. The required power for wind speed is a maximum value at $\omega_{t,opt}$. This is the speed which corresponds to λ_{opt} and $C_{p,max}$. To obtain the maximum power, the turbine must work at λ_{opt}. This is available by controlling the rotational speed of the turbine in order to rotate at the optimum speed of rotation. The points of maximum power curve are obtained as illustrated in Figure 3.

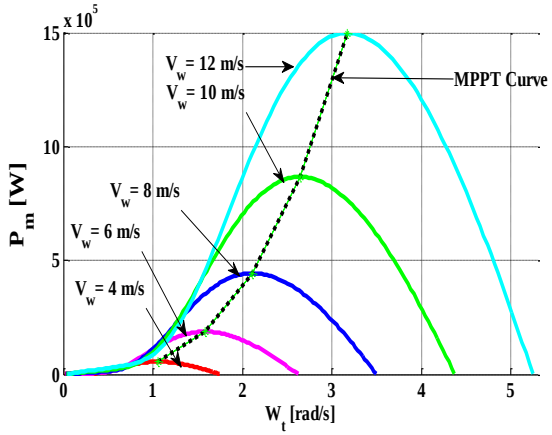

Fig. 3 Output mechanical power of 1.5 MW DFIG turbine and MPP versus turbine speed at various wind speed.

4. MPPT based optimal TSR technique

For MPPT the optimal TSR λ_{opt} is measured at maximum power coefficient $C_{p,max}$ and zero pitch angle β by using equation (2). Equation (2) is optimized for various λ using optimization method called Genetic Algorithm (GA) in present work. The next section will describe the GA method.

5. Genetic algorithm optimization

The GA based on natural selection is a powerful optimization technique [15], [16], [17], [18]. Optimizing functions called fitness functions is the main aim of GA. The GA controller is used in the region between the cut-in speed and the rated wind speed to find the maximum power at various wind speed. To get and track the maximum power point, it must get the optimal value of λ at maximum power coefficient and this is done by GA to solve equation (2) at various values of λ. Where the pitch angle β is zero in this region. The object function used in this work is one variable equation, then it is necessary to define constraints and the other required parameters of GA as the following:

$$0 \leq \lambda \leq 13$$

Where $\lambda_{min} = 0$ and $\lambda_{max} = 13$. The parameters for GA are given in Table 2.

Table 2
Parameters of GA

GA property	Value
Chromosome Length	16
Population Size	200
No. of iterations (Generations)	150

The object function is given as in equation (5):

$$C_p(\lambda) = 0.5176\left(\frac{116}{\lambda_i} - 5\right)e^{-\frac{21}{\lambda_i}} + 0.0068\lambda \qquad (5)$$

Where $\frac{1}{\lambda_i} = \frac{1}{\lambda} - 0.035$ at $\beta = 0$. Then, the above equation is entered in the GA under mentioned conditions and the result value obtained after number of generations (Iterations) of power coefficient using GA is $C_{p,max} = 0.48$ as depicted in Figure 4. The TSR λ corresponding to $C_{p,max}$ is $\lambda_{opt} = 8.1$ is illustrated in Figure 5.

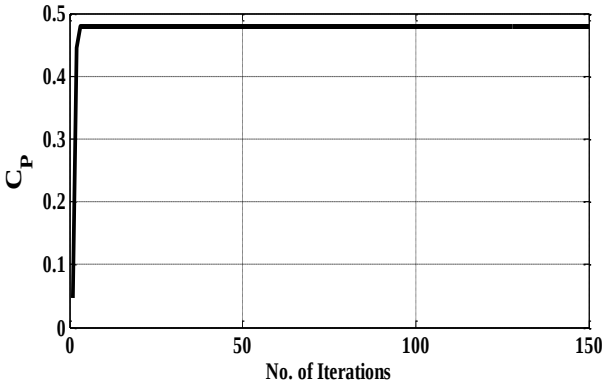

Fig. 4 Maximum power coefficient $C_{p,max}$ versus number of iterations.

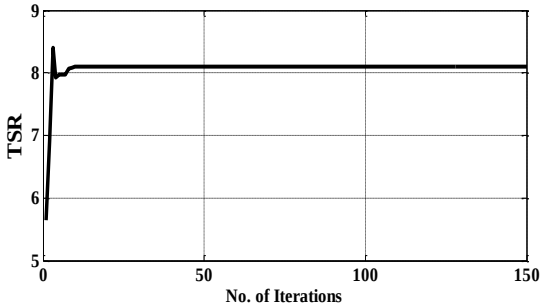

Fig. 5 Optimal value of TSR λ versus number of iterations.

So, it is important to get ω_t which is corresponding to λ_{opt} at different wind speed at specified ω_t corresponding to the maximum power that can be obtained using equation (1) as illustrated in Figure 3. The wind turbine parameters used in this work are shown in Table 3.

Table 3
Parameters of wind turbine

Parameter	Symbol	Value and Units
Air density	ρ	1.225 Kg/m^3
Number of blades	N_{blades}	3
Rated wind speed	$V_{\text{Rated}-\text{wind}}$	12 m/sec
Cut-in/out wind speed	$V_{cut-in}/V_{cut-out}$	4/24 m/sec
Rated Power	P_{rated}	1.5 MW
Blade length	R	30.6567m
Gearbox ratio	R_{GB}	57.7996
Max $\mathbf{C_p}$ (MPPT)	C_{pmax}	0.48
Optimal λ (MPPT)	λ_{opt}	8.1

6. Model of DFIG based WECS

The structure of 1.5 MW DFIG is illustrated in Figure 6. The dynamics of 1.5 MW DFIG are represented by state space model (fourth order) using the d-q synchronous reference frame as described in equations (6)-(9) [5]. Where v_{sq}, v_{sd}, $v_{rq}$and v_{rd} are the q and d-axis stator and rotor voltages, respectively. i_{sq} , i_{sd} , i_{rq} and i_{rd} are the q and d-axis stator and rotor currents, respectively. λ_{sq} , λ_{sd} , λ_{rq} and λ_{rd} are the q and d-axis stator and rotor fluxes, respectively.

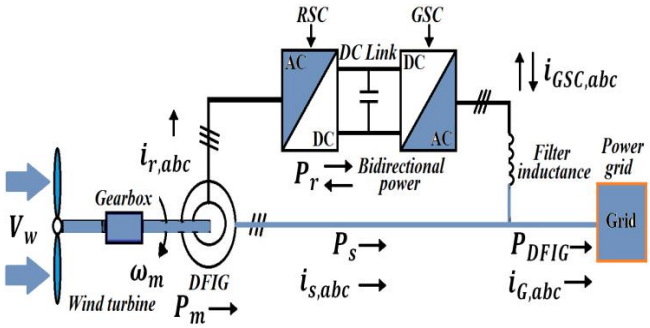

Fig. 6 DFIG wind turbine based WECS.

$$v_{sq} = R_s i_{sq} + \omega_e \lambda_{sd} + \frac{d}{dt}\lambda_{sq} \quad (6)$$

$$v_{sd} = R_s i_{sd} - \omega_e \lambda_{sq} + \frac{d}{dt}\lambda_{sd} \quad (7)$$

$$v_{rq} = R_r i_{rq} + (\omega_e - \omega_r)\lambda_{rd} + \frac{d}{dt}\lambda_{rq} \quad (8)$$

$$v_{rd} = R_r i_{rd} - (\omega_e - \omega_r)\lambda_{rq} + \frac{d}{dt}\lambda_{rd} \quad (9)$$

Where R_s and R_r are the stator and rotor resistances, respectively. The flux linkage equations are described as in equations (10)-(13):

$$\lambda_{sq} = L_s i_{sq} + L_m i_{rq} \quad (10)$$

$$\lambda_{sd} = L_s i_{sd} + L_m i_{rd} \quad (11)$$

$$\lambda_{rq} = L_r i_{rq} + L_m i_{sq} \quad (12)$$

$$\lambda_{rd} = L_r i_{rd} + L_m i_{sd} \quad (13)$$

Where L_s , L_r and L_m are the stator, rotor and mutual inductances, respectively, with $L_s = L_{ls} + L_m$ and $L_r = L_{lr} + L_m$; L_{ls} and L_{lr} are the stator and rotor self-inductance, respectively. All the equations mentioned above represent induction motor equations. When the induction motor works as a generator, the current direction will be opposite. The active and reactive power outputs from stator and rotor side are described as in equations (14)-(17):

$$P_s = \frac{3}{2}\left(v_{sq} i_{sq} + v_{sd} i_{sd}\right) \quad (14)$$

$$Q_s = \frac{3}{2}\left(v_{sq} i_{sd} - v_{sd} i_{sq}\right) \quad (15)$$

$$P_r = \frac{3}{2}\left(v_{rq} i_{rq} + v_{rd} i_{rd}\right) \quad (16)$$

$$Q_r = \frac{3}{2}\left(v_{rq} i_{rd} - v_{rd} i_{rq}\right) \quad (17)$$

The total active and reactive powers produced by DFIG are described as in equations (18)-(19):

$$P_{total} = P_{DFIG} = P_s + P_r \quad (18)$$

$$Q_{total} = Q_s + Q_r \quad (19)$$

If total P_{total} and/or total Q_{total} is negative, DFIG is giving power to the power grid, else it is taking power from the grid. The electromagnetic torque T_e produced by the machine which can be in terms of currents and flux linkages is given as in equation (20):

$$T_e = \frac{3*P}{2}\left(\lambda_{sd} i_{sq} - \lambda_{sq} i_{sd}\right) \quad (20)$$

Where P is the number of the pole pairs.

7. Control scheme of DFIG based WECS

Control of the 1.5 MW DFIG is done by control of the power converter, which contains control of the RSC and control of the Grid Side Converter (GSC) as the following:

A. Design of RSC controller for proposed genetic MPPT

In DFIG wind turbine system, the stator is directly connected to the power grid; its voltage and frequency are constant under the normal operating conditions. Therefore, Stator Voltage Oriented Control (SVOC) is used for the DFIG [14]. The stator voltage oriented control is done by aligning the d-axis of the synchronous reference frame with the stator voltage v_s. The resultant d- and q-axis stator voltages are: $v_{sq} = 0$ and $v_{sd} = v_s$. This DFIG control circuit is rotor side control scheme where the active power is controlled by the direct current axis loop and the stator reactive power is controlled by the quadrature current axis loop. In the active power control loop the rotor electrical angular speed is compared with the reference rotor electrical angular speed obtained by MPPT. Then, the error is fed to a conventional PI (Speed Regulator) controller to generate the reference direct axis current. Where, the proportional gain $K_{P,\omega r}$ and the integral gain $K_{I,\omega r}$ of the speed regulator are shown in Table 4. Similarly, the stator side reactive power is calculated and is compared with the reference stator reactive power ($Q_{s,ref}$ =0). Then, the error is fed to another PI (Var Regulator) controller to produce the reference quadrature axis current. Where, the proportional gain $K_{P,Qs}$ and the integral gain $K_{I,Qs}$ of the var regulator are illustrated in Table 4. The method used in evaluation of these parameters is illustrated in details in section 10. Then, both of the direct i_{rd}^* and quadrature i_{rq}^* axis reference currents are converted from d-q axis reference frame to a-b-c frame. Then, the three phase reference currents are compared with three phase rotor actual currents. Then, the error is the input to hysteresis current controller. Finally, the output of this controller is the switch control signals to the firing gate of RSC. The hysteresis controller output provides the switching pulses for the rotor side bidirectional converter control as shown in Figure 7. The overall control scheme is implemented using MATLAB /Simulink as shown in Figure 8. The stator voltage vector angle θ_s is measured as shown in Figure 9 and the rotor position angle θ_r is determined by an encoder mounted on the generator shaft. The slip angle θ_{sl} for the reference frame transformation can be obtained as the following ($\theta_{sl} = \theta_s - \theta_r$) as shown in Figure 9.

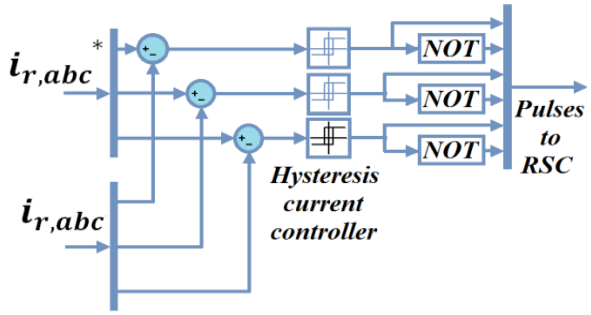

Fig. 7 Hysteresis current controller.

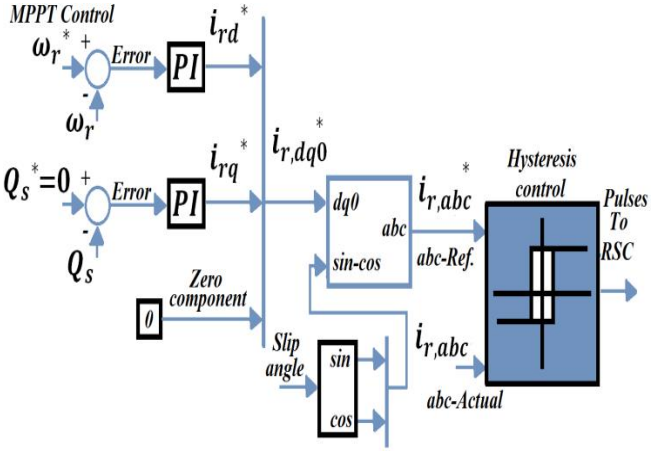

Fig. 8 Block diagram of RSC.

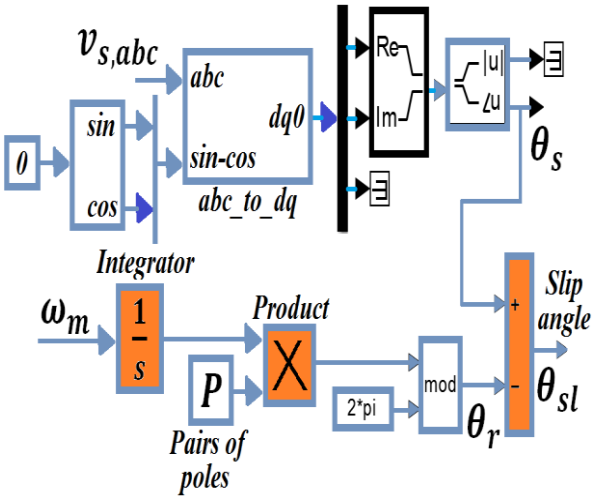

Fig. 9 Block diagram of slip angle calculator.

Table 4
Parameters of the speed and var regulators

Gains of the speed regulator	Values
f_{sw}	$1000\ Hz$
ω_{sw}	$2\pi f_{sw}$
ω_{outer}	$\omega_{sw}/100$
$\omega_{0\omega r}$	$\omega_{outer}/100$
$\mathbf{K_{P,\omega r}}$	$\sqrt{2}\omega_{0\omega r}\frac{J}{P}$
$\mathbf{K_{I,\omega r}}$	$\frac{J}{P}{\omega_{0\omega r}}^2$
ω_{0Qs}	ω_{outer}
$K_{P,Qs}$	$\sqrt{2}\,\omega_{0Qs}\,C_{Qs}$
$K_{I,Qs}$	$C_{Qs}\,{\omega_{0Qs}}^2$

Where C_{Qs} is a constant and its value is $C_{Qs} = \frac{2\,\sigma\,L_s\,L_r}{3\,\omega_e\,L_m} = Const.$ Noting that the switching frequency has the same value in the all parts of this paper. Also, the angular switching frequency is assumed to be 100 times outer loop controller.

B. Design of GSC controller

The objective of the GSC control system is to make the DC-link voltage constant at the required level for RSC, while the main input currents must be sinusoidal and in phase with their counterpart voltages, for which the control system of DFIG achieves unity power factor condition. The proposed control algorithm of GSC adopts the SVO to regulate DC-Link voltage and achieve a unity power factor. This strategy leads to get and control the following active and reactive component fed to grid. This DFIG control scheme allows controlling the DC-link voltage which is controlled by the direct current axis loop and the quadrature current axis which is kept at zero for unity power factor. The actual DC-link voltage is compared with the reference DC-link voltage and the error is fed to a conventional PI (DC Voltage Regulator) controller to generate the reference direct axis current $i_{GSC,d}{}^{*}$. Where, the proportional gain $K_{P,dc}$ and the integral gain $K_{I,dc}$ of the DC voltage regulator are described in Table 5. The strategy applied in estimation of these parameters is shown in details in section 10. Then, both of the direct $i_{GSC,d}{}^{*}$ and quadrature $i_{GSC,q}{}^{*} = 0$ axis reference currents are converted from d-q axis reference frame to a-b-c frame. Then, the three phase reference currents are compared with three phase GSC actual currents. Then, the error is the input to hysteresis current controller. Finally, the output of this controller is the switch control signals to the firing gate of GSC. The hysteresis controller output produces the switching pulses for the grid side bidirectional converter control as shown in Figure 10.

Table 5
Parameters of DC-link voltage regulator

Gains of DC voltage regulator	Values
ω_{0dc}	ω_{outer}
$K_{P,dc}$	$\sqrt{2}\omega_{0dc}\, C$
$K_{I,dc}$	$C\ \omega_{0dc}{}^{2}$

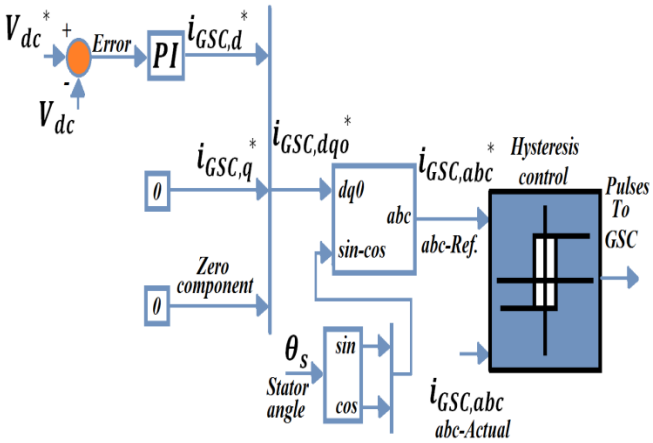

Fig. 10 Block diagram of GSC.

8. Connecting DFIG wind turbine to power grid without incidence of grid disturbances

The 1.5 MW DFIG-based WECS is connected to power grid under normal operating conditions without any grid disturbances. Under varying the wind speed as illustrated in the next sections, the rotor mechanical speed and the output power of DFIG wind turbine will be varied as depicted in Figure 11a and Figure 11b, respectively. Noting that the output power of DFIG with minus signal means that DFIG wind turbine is in generation mode.

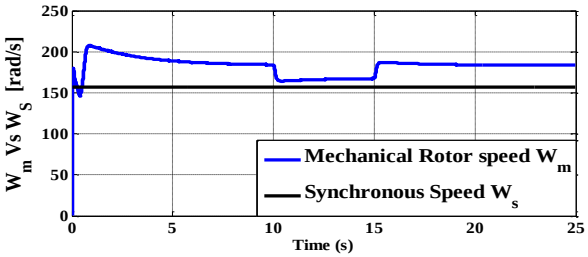

(a)

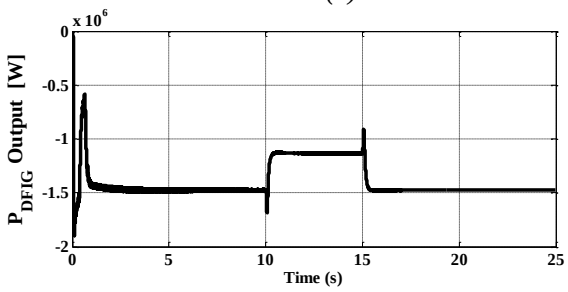

(b)

Fig. 11 The DFIG wind turbine
(a) Mechanical rotor speed versus synchronous speed, (b) Output power.

9. Occurrence of grid disturbances at the PCC with DFIG without connecting STATCOM and SAPF

The 1.5 MW DFIG-based WECS with connecting the sudden load at PCC is shown in Figure 12a. The system is executed for two cases of the sudden load for different wind speed and also for another case under occurrence of three phase fault in transmission line as depicted in Figure 12b. Noting that the three phase fault is through ground resistance R_g and each phase of the three phase fault has a resistance called phase fault breaker R_{on} as illustrated in Figure 12c.

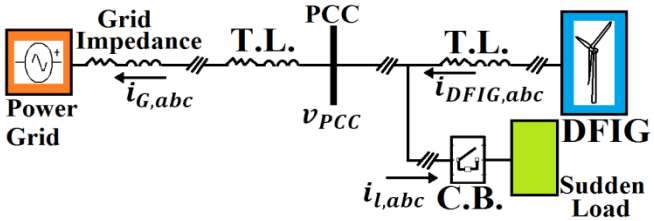

(a)

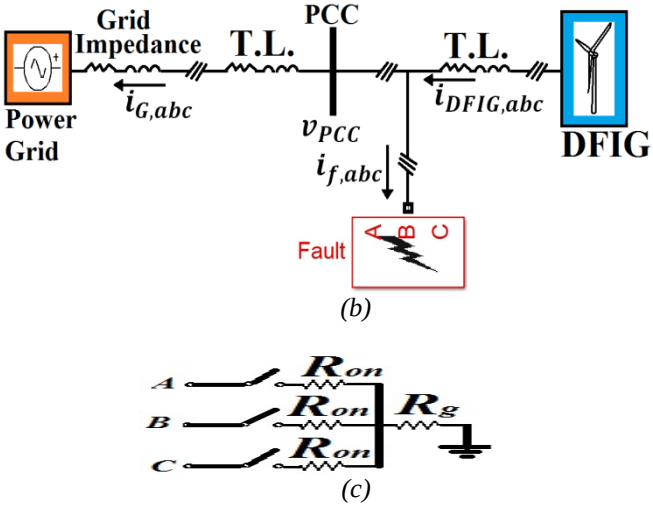

Fig. 12 At PCC in the overall model
(a) For connecting the sudden load, (b) For occurrence of three phase fault, (c) Three phase fault connection circuit

Firstly, in the cases of connecting the sudden inductive load at PCC and happening of three phase fault in transmission line, the effect of voltage sag is appeared as shown in Figure 13 and Figure 14, respectively. Secondly, the case for connecting the sudden capacitive load, the effect of voltage swell is illustrated in Figure 15. In all cases the wind speed is varied as illustrated in Figure 16.

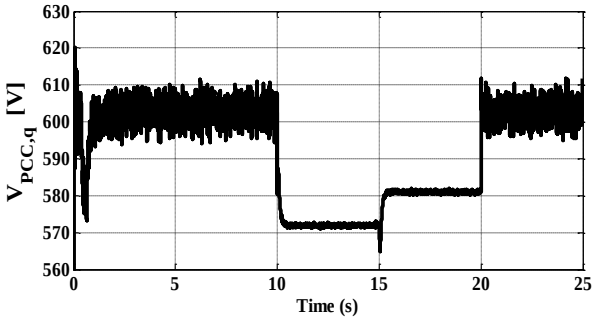

Fig. 13 The PCC voltage sag during connecting sudden inductive load at the DFIG wind turbine without STATCOM and SAPF.

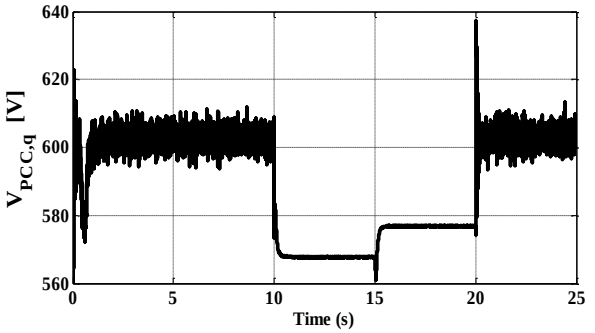

Fig. 14 The PCC voltage $v_{PCC,q}$ sag during occurrence of three phase fault at the DFIG wind turbine without STATCOM and SAPF

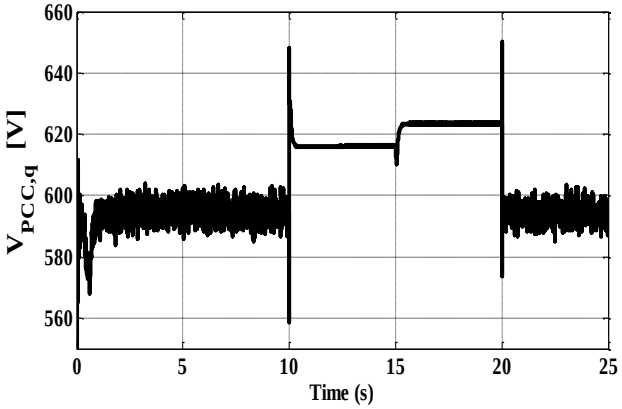

Fig. 15 The PCC voltage swell during connecting of sudden capacitive load at the DFIG wind turbine without STATCOM and SAPF

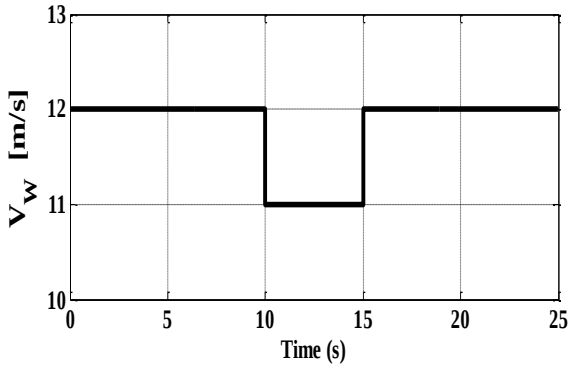

Fig. 16 Wind speed variation.

10. Control design of STATCOM

STATCOM based power electronics is three phase shunt connected device. It is connected near from the load at PCC. The main components of STATCOM with DFIG are connected in power distribution system as illustrated in Figure 17. It consists of DC-link charged capacitor, three phase converter IGBT switches, AC filter is a small filter capacitor C_m is also connected in parallel to the same bus for eliminating harmonics, coupling transformer and a control method [19], [20], [21]. The electronic diagram of STATCOM is the voltage source converter which converts the DC voltage into AC three phase output voltages at fundamental frequency. The controller of the STATCOM is used to operate the converter where the phase angle between the converter voltage and the line voltage is dynamically adjusted so that the STATCOM can generate or absorb the desired reactive power in VAR at PCC. The objective of STATCOM is to regulate the voltage magnitude at the PCC bus within a desired range by exchanging the reactive power with the distribution system. At the same time the converter in STATCOM must maintain the DC-link voltage constant.

STATCOM is modeled as Pulse Width Modulation (PWM) converter; the dynamic equations of STATCOM

in d-q axis reference frame are described as in equations (21) and (22), respectively.

$$\begin{cases} v_{stat,d} = R_{stat} i_{stat,d} + L_{stat} \dfrac{di_{stat,d}}{dt} - \omega_e L_{stat} i_{stat,q} \\ \qquad +v_{PCC,d} \\ v_{stat,d} = \dfrac{M_{stat,d} V_{dc}}{2} \end{cases} \tag{21}$$

$$\begin{cases} v_{stat,q} = R_{stat} i_{stat,q} + L_{stat} \dfrac{di_{stat,q}}{dt} + \omega_e L_{stat} i_{stat,d} \\ \qquad +v_{PCC,q} \\ v_{stat,q} = \dfrac{M_{stat,q} V_{dc}}{2} \end{cases} \tag{22}$$

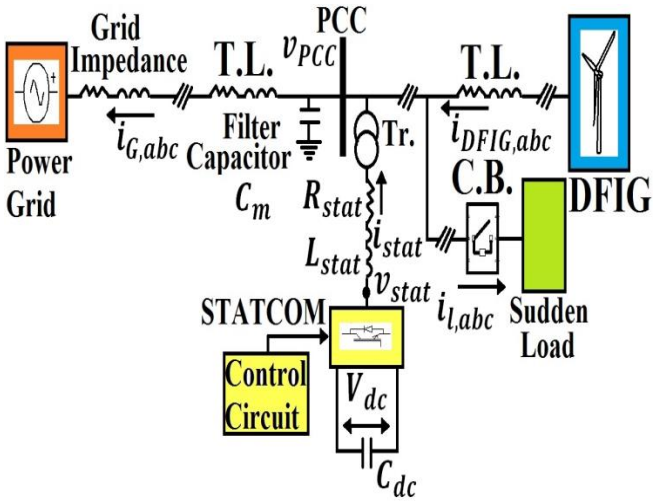

Fig. 17 STATCOM with DFIG in power system.

Where R_{stat} and L_{stat} are line resistance and inductance, respectively. V_{dc} is the DC-link voltage. STATCOM DC voltage dynamics in DC-link is described as in equation (23) [19].

$$C_{dc} \frac{dV_{dc}}{dt} = \frac{-3}{4}\left(M_{stat,q} i_{stat,q} + M_{stat,d} i_{stat,d}\right) \tag{23}$$

The voltage magnitude (v_{PCC}) at the PCC is described as in equation (24).

$${v_{PCC}}^2 = {v_{PCC,d}}^2 + {v_{PCC,q}}^2 \tag{24}$$

By differentiating equation (24) with respect to time as the following:

$$\frac{d{v_{PCC}}^2}{dt} = 2v_{PCC,d} \frac{dv_{PCC,d}}{dt} + 2v_{PCC,q} \frac{dv_{PCC,q}}{dt} \tag{25}$$

Equation (25) describes the square of voltage magnitude dynamics at the PCC and this voltage magnitude will be $v_{PCC} = \left|\sqrt{{v_{PCC}}^2}\right|$. For the DC voltage control, equation (23) can be rewritten as:

$$-\frac{4}{3} C_{dc} \frac{dV_{dc}}{dt} = \left(M_{stat,q} i_{stat,q} + M_{stat,d} i_{stat,d}\right) = \alpha_{dc} = K_{dc}({V_{dc}}^* - V_{dc}) \tag{26}$$

Where K_{dc} is the DC voltage regulator given as $K_{dc} = \left(K_{P,dc} + \frac{K_{I,dc}}{s}\right)$. Then, equation (26) will be:

$$\frac{4}{3} C_{dc} \frac{dV_{dc}}{dt} = \alpha_{dc} = \left(K_{P,dc} + \frac{K_{I,dc}}{s}\right){V_{dc}}^* - \left(K_{P,dc} + \frac{K_{I,dc}}{s}\right) V_{dc} \tag{27}$$

Then, it is required to get the transfer function for DC voltage regulator as described below:

$$\frac{V_{dc}}{{V_{dc}}^*} = \frac{\frac{3}{4C_{dc}}\left(s\, K_{P,dc} + K_{I,dc}\right)}{s^2 + s\,\frac{3}{4C_{dc}} K_{P,dc} + \frac{3}{4C_{dc}} K_{I,dc}} \tag{28}$$

The PI parameters of DC voltage controller are determined by comparing the coefficients in equation (29) with the denominator of the corresponding transfer function in equation (28) as described in Table 6. After comparison in the outer loop of STATCOM design, the PI parameters of DC voltage regulator will be:

$$s^2 + \sqrt{2}\,\omega_0 s + {\omega_0}^2 = 0 \tag{29}$$

Where $s = \frac{d}{dt}$ and ω_0 is the bandwidth frequency.

Table 6
Parameters of STATCOM for DC voltage regulator

Gains	Values
$\boldsymbol{\omega_{0dc}}$	ω_{outer}
$\boldsymbol{K_{P,dc}}$	$\frac{4}{3}\sqrt{2}\,\omega_{0dc}\,C_{dc}$
$\boldsymbol{K_{I,dc}}$	$\frac{4}{3} C_{dc}\,{\omega_{0dc}}^2$

For voltage magnitude control from Figure 18, the dynamic voltage equations at the PCC can be written as:

$$C_m \frac{dv_{PCC,d}}{dt} = i_{stat,d} - i_{Gd} + \omega_e C_m v_{PCC,q} \tag{30}$$

$$C_m \frac{dv_{PCC,q}}{dt} = i_{stat,q} - i_{Gq} - \omega_e C_m v_{PCC,d} \tag{31}$$

Substituting equations (30) and (31) into equation (25) gives:

$$\frac{C_m}{2} \frac{d{v_{PCC}}^2}{dt} = v_{PCC,d}\left(i_{stat,d} - i_{Gd}\right) + v_{PCC,q}\left(i_{stat,q} - i_{Gq}\right) = \alpha_{PCC} = K_{PCC}\left({v_{PCC}}^{2^*} - {v_{PCC}}^2\right) \tag{32}$$

Where K_{PCC} is the PI controller for voltage magnitude control given as $K_{PCC} = \left(K_{P,PCC} + \frac{K_{I,PCC}}{s}\right)$. Substituting for K_{PCC} results in equation (33) and from which the transfer function is found as described in equation (34).

$$\frac{C_m}{2}\frac{d{v_{PCC}}^2}{dt} = \left(K_{P,PCC} + \frac{K_{I,PCC}}{s}\right){v_{PCC}}^{2^*} - \left(K_{P,PCC} + \frac{K_{I,PCC}}{s}\right){v_{PCC}}^2 \quad (33)$$

$$\frac{{V_{PCC}}^2}{{V_{PCC}}^{2^*}} = \frac{\frac{2}{C_m}(s\,K_{P,PCC}+K_{I,PCC})}{s^2+s\,\frac{2}{C_m}K_{P,PCC}+\frac{2}{C_m}K_{I,PCC}} \quad (34)$$

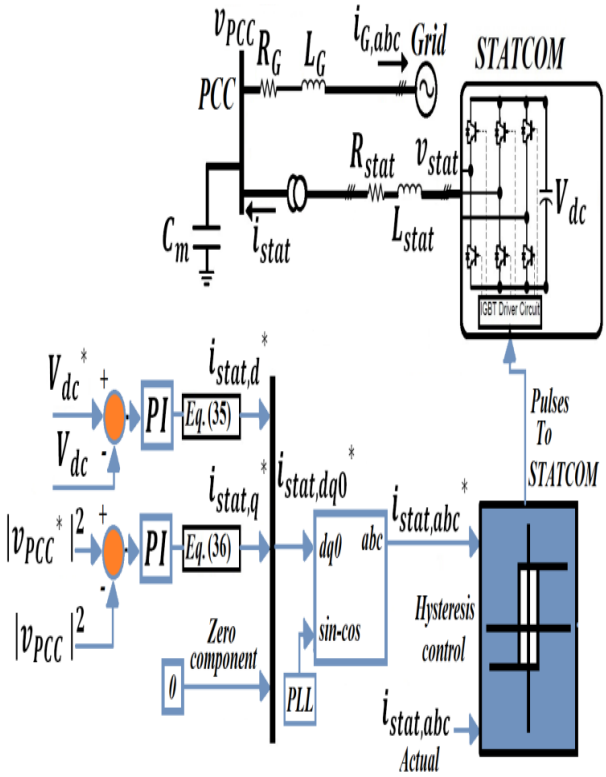

Fig. 18 STATCOM controller.

The PI parameters of voltage magnitude controller are determined by comparing the coefficients in equation (29) with the denominator of the corresponding transfer function in equation (34) as illustrated in Table 7. For the outer loop in STATCOM design $\omega_{0PCC} = \omega_{outer} = 62.8\ rad/s$ after comparison the PI parameters of voltage magnitude regulator will be:

Table 7
Parameters of STATCOM for voltage magnitude regulator

Gains	Values
$\boldsymbol{\omega_{0PCC}}$	ω_{outer}
$\boldsymbol{K_{P,PCC}}$	$\sqrt{2}\,\omega_{0PCC}\,\frac{C_m}{2}$
$\boldsymbol{K_{I,PCC}}$	$\frac{C_m}{2}\,{\omega_{0PCC}}^2$

Where ω_{0PCC} is the bandwidth of the voltage magnitude controller. Finally, the d-q axis current of STATCOM ${i_{stat,d}}^*$ and ${i_{stat,q}}^*$ are obtained by using equations (26) and (32) as illustrated in Figure 18. The currents ${i_{stat,d}}^*$ and ${i_{stat,q}}^*$ are described below:

$${i_{stat,d}}^* = \frac{1}{M_{stat,d}}\left(\alpha_{dc} - M_{stat,q}\,i_{stat,q}\right) \quad (35)$$

$${i_{stat,q}}^* = \frac{1}{v_{PCC,q}}\left(\alpha_{PCC} - v_{PCC,d}\left(i_{stat,d} - i_{Gd}\right)\right) + i_{Gq} \quad (36)$$

Figure 18 shows the control circuit of STATCOM. The proposed control circuit of STATCOM adopts its PLL by using the required angle θ circuit to regulate DC-link voltage and the terminal voltage at PCC. Where the PLL circuit is done by aligning the q-axis of the synchronous reference frame with the voltage v_{PCC}. The parameters of PI controller in PLL circuit are proportional gain $K_{P,pll,stat}$ and integral gain $K_{I,pll,stat}$ that illustrated in Table 8. The resultant d-q axis voltages at PCC are: $v_{PCC,d}$ =0 and $v_{PCC,q} = v_{PCC}$ as illustrated in Figure 19.

Table 8
Parameters of STATCOM for PLL regulator

Gains	Values
$\boldsymbol{\omega_0}$	$\omega_{sw}/15$
$\boldsymbol{K_{P,pll,stat}}$	$\sqrt{2}\,\omega_0/v_s$
$\boldsymbol{K_{I,pll,stat}}$	${\omega_0}^2/v_s$

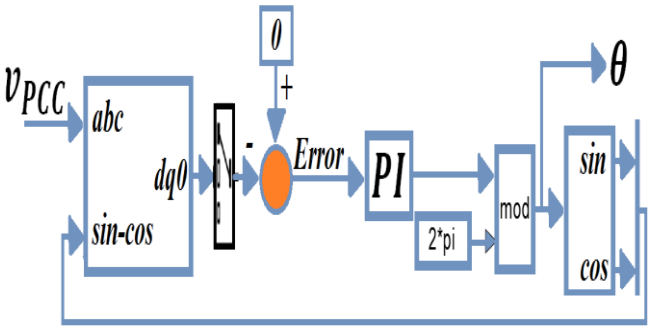

Fig. 19 PLL circuit for STATCOM controller.

This STATCOM allows controlling the DC-link voltage which is controlled by the direct current axis loop ${i_{stat,d}}^*$ and the magnitude of terminal voltage at PCC which is controlled by the quadrature current axis loop ${i_{stat,q}}^*$. The actual DC-link voltage is compared with the reference DC-link voltage and the error is fed to a conventional PI (DC voltage control) controller to generate the reference direct axis current ${i_{stat,d}}^*$. Similarly, The square actual voltage magnitude at PCC is compared with the square reference voltage magnitude and the error is fed to a conventional PI (voltage magnitude control) controller to generate the reference quadrature axis current ${i_{stat,q}}^*$. Then, both of the

direct $i_{stat,d}{}^{*}$and quadrature $i_{stat,q}{}^{*}$axis reference currents are converted from d-q axis reference frame to a-b-c frame. Then, the three phase reference currents are compared with three phase STATCOM actual currents. Then, the error is the input to hysteresis current controller. Finally, the output of this controller is the switch control signals to the firing gates of STATCOM converter.

11. Configuration and control design of SAPF

The present work tries to apply SAPF for voltage terminal regulation of DFIG for different sudden loads such as inductive load (for voltage sag effect) and capacitive load (for voltage swell effect) for power quality improvement where the sudden load is connected to PCC through circuit breaker as shown in Figure 20. Frequency domain compensation based on Fourier analysis, is not common because it requires much real time processing power. There are several methods to define the harmonic currents, phase shift and voltage control, the most classical methods are instantaneous power theory p-q, d-q synchronous detection method and Fryze current control [22], [23], [24], [25], [26]. It is known that the role of SAPF with DFIG connected to three phase balanced power grid and balanced sudden load consuming or supplying reactive power which causes voltage sag or swell is voltage terminal regulation. In this work, the synchronous reference frame d-q axis is used as shown in Figure 21. Practically, the load currents of the sudden load in a-b-c frame (i_{La}, i_{Lb} and i_{Lc}) are obtained by using current sensors. After that, the load currents in a-b-c frame are transformed into d-q-0 axis reference frame (i_{Ld}, i_{Lq} and i_{L0}) according to the same previous PLL circuit design as given in equation (37).

$$\begin{bmatrix} i_{Ld} \\ i_{Lq} \\ i_{L0} \end{bmatrix} = \sqrt{\frac{2}{3}} \begin{bmatrix} \cos(\omega t) & \cos(\omega t - 120^o) & \cos(\omega t + 120^o) \\ -\sin(\omega t) & -\sin(\omega t - 120^o) & -\sin(\omega t + 120^o) \\ \frac{1}{\sqrt{2}} & \frac{1}{\sqrt{2}} & \frac{1}{\sqrt{2}} \end{bmatrix} \begin{bmatrix} i_{La} \\ i_{Lb} \\ i_{Lc} \end{bmatrix} \quad (37)$$

Where ωt is the phase of the positive sequence of the system voltage and it is provided by PLL circuit. Then, a High Pass Filter (HPF) is used in both d and q axis to get the high frequency components of the load current ($i_{Ld}^{\sim}$ and $i_{Lq}^{\sim}$) as follows:

$$i_{Ld}(t) = I_{Ld}(t) + i_{Ld}^{\wedge}(t) + i_{Ld}^{\sim}(t) \quad (38)$$

$$i_{Lq}(t) = I_{Lq}(t) + i_{Lq}^{\wedge}(t) + i_{Lq}^{\sim}(t) \quad (39)$$

Then, the high frequency component will be subtracted from the total current in both d and q axis (i_{Ld} and i_{Lq}). Noting that I_{Ld} and $I_{Lq}$are the DC components of the load current in d-q axis (small values are neglected). Finally, the only remain component is the reference compensation low frequency component of the load current in both d and q axis ($i_{Ld}^{\wedge}$ and $i_{Lq}^{\wedge}$). The compensation reference currents in d-q axis and will be converted into a-b-c frame as given in equation (40).

$$\begin{bmatrix} i_{aref} \\ i_{bref} \\ i_{cref} \end{bmatrix} = \sqrt{\frac{2}{3}} \begin{bmatrix} \cos(\omega t) & -\sin(\omega t) \\ \cos(\omega t - 120^o) & -\sin(\omega t - 120^o) \\ \cos(\omega t + 120^o) & -\sin(\omega t + 120^o) \end{bmatrix} \begin{bmatrix} i_{Ld}^{\wedge} \\ i_{Lq}^{\wedge} \\ i_0 \end{bmatrix} \quad (40)$$

After that, the compensation reference currents will be compared with the compensation actual current of SAPF through hysteresis current controller where the output of this controller is the switch control signals to the inverter of SAPF as shown in Figure 20 and Figure 21. Noting that in Figure 20 a filter inductance is used at the output of the inverter of SAPF to eliminate the distortion produced by switches in the inverter circuit of SAPF. Also, a DC constant voltage source is used in the DC side of the inverter circuit of SAPF.

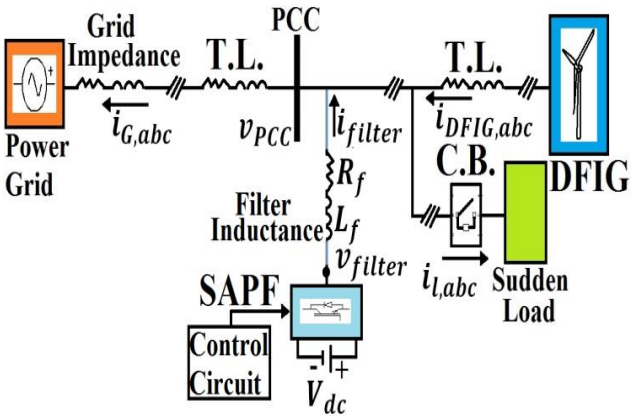

Fig. 20 SAPF with DFIG in power system.

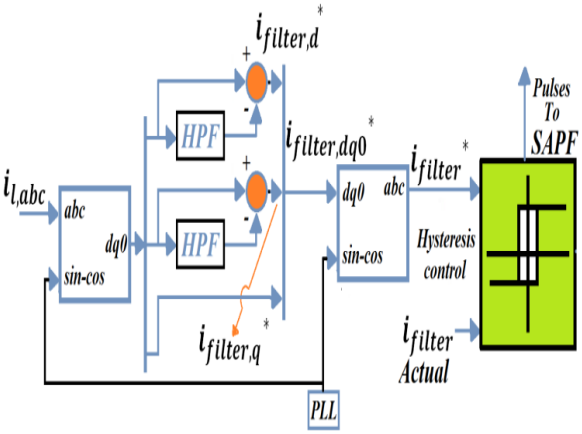

Fig. 21 Block diagram of SAPF controller.

Where $i_{filter,d}{}^{*}$and $i_{filter,q}{}^{*}$are the compensation reference currents in d and q axis, respectively.

12. Design of PI Controller for DFIG and STATCOM

The output signal of a PI controller is obtained by using equation (41):

$$U = K_P * e + K_I \int e * dt \quad (41)$$

Where e, K_P and K_I are the error signal, the proportional gain and integral gain, respectively. Some methods are used to measure the parameters of the system that can save the overall system in the stable zone. Butterworth polynomial method is used here to optimize the closed loop eigenvalue locations [27]. The Butterworth method locates the eigenvalues uniformly in the left half s-plane (stable area) on a circle with radius ω_o, with its center at the origin as illustrated in Figure 22.

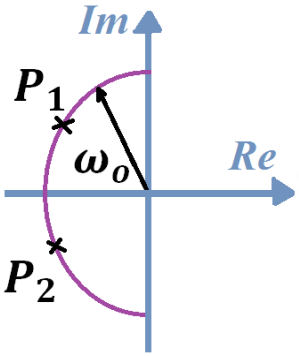

Fig. 22 Location of poles in left half s-plane using Butterworth polynomial.

The Butterworth polynomial for transfer function with second order denominator is described as in equation (29). The PI parameters are measured by comparing the coefficients in equation (29) with the denominators of the corresponding transfer functions and then selecting appropriate ω_o . Where ω_o is the bandwidth of the controller, which depends on the design value. The parameters of each PI controller used in controlling of DFIG and STATCOM are shown in Table 9.

Table 9
Parameters of PI controllers

Converter	Regulator	Symbol	Value
RSC	Speed Regulator	$K_{P,\omega r}$	17.7715
		$K_{I,\omega r}$	7.8957
	Var Regulator	$K_{P,Qs}$	$5.7798*10^{-5}$
		$K_{I,Qs}$	0.0026
GSC	DC Voltage Regulator	$k_{P,dc}$	79.9719
		$k_{I,dc}$	3553.1
	DC Voltage Regulator	$K_{P,dc}$	106.6292
		$K_{I,dc}$	4737.4
STATCOM	AC Voltage Regulator	$K_{P,pcc}$	0.2444
		$K_{I,pcc}$	10.8566
	PLL Circuit	$K_{P,pll,stat}$	1.0466
		$K_{I,pll,stat}$	309.9994

13. Digital simulation results of the overall system

The overall model is simulated two times, the first time was for STATCOM and the second time was for SAPF under the same load and fault conditions as illustrated in Figure 17 and Figure 20, respectively. The main whole model consists of DFIG wind turbine control structure, transmission line and power grid under connecting the balanced sudden load at PCC and occurrence of three phase fault as a grid disturbance. Where the DFIG wind turbine is used to supply the sudden load with the needed power and the remained power is supplied to the power grid. The sudden inductive load and the occurrence of three phase fault are used as a grid disturbance to show and appear the effect of voltage sag. The sudden inductive load is three phase inductive load ($R_{load} = 0.6\,\Omega$ and $L_{load} = 9\,\mu H$) connected to PCC through circuit breaker. The three phase fault is through ground resistance $R_g = 0.001\,\Omega$ and each phase of the three phase fault has a resistance called phase fault breaker $R_{on} = 0.5\,\Omega$. The sudden capacitive load is used as a grid disturbance to indicate the effect of voltage swell. The sudden capacitive load is a three phase capacitive load ($R_{load} = 1\,m\Omega$ and $C_{load} = 5\,mF$) connected to PCC through circuit breaker. The initial status of the circuit breaker at the terminals of the sudden load is normally open and its transition time is from 10 sec to 20 sec of simulation time. The overall model is implemented in MATLAB /Simulink package. The DFIG parameters are shown in Table 10. The simulation for all cases is carried out for the same mentioned varied wind speed and the digital simulation results will be displayed for three cases as the following:

1) Comparison between STATCOM and SAPF connected at PCC under presence of sudden inductive load.
2) Comparison between STATCOM and SAPF connected at PCC under occurrence of three phase fault.
3) Comparison between STATCOM and SAPF connected at PCC under existence of sudden capacitive load.

Table 10
DFIG parameters

Parameter	Value
$P_{m,rated}$	1.5 MW
Rated stator line voltage	690 V (rms)
Rated stator frequency	50 Hz
Rated rotor speed	1750 rpm
P	2
$T_{m,rated}$	8.185 kN-m
R_s	2.65 $m\Omega$
R_r	2.63 $m\Omega$
L_{ls}	0.1687 mH
L_{lr}	0.1337 mH
L_m	5.4749 mH
J	20 $Kg.m^2$
V_{dc}	1600 V
C	900 mF

Noting that, STATCOM is connected in parallel with the grid disturbance at PCC. The STACOM parameters are shown in Table 11.

Table 11
STATCOM parameters

Parameters	Value
Capacitor voltage $\mathbf{V_{dc}}$	1100 V
Line inductance	1 mH
Line resistance	0.1 Ω
DC-link capacitance	0.9 F
Filter capacitor	5.5 mF

Under the same conditions mentioned above the SAPF is used instead of STATCOM. The SAPF is connected in parallel with the grid disturbance at PCC for the same wind speed of DFIG wind turbine. The SAPF parameters are shown in Table 12.

Table 12
SAPF parameters

Parameters	Value
DC side voltage $\mathbf{V_{dc}}$	1100 V
Filter inductance	1 mH
Filter resistance	1 mΩ

A. Comparison between STATCOM and SAPF connected at PCC under presence of sudden inductive load

Firstly, the overall model is simulated in presence of sudden inductive load as a grid disturbance in the period from 10 seconds to 20 seconds without using STATCOM as a result the PCC voltage is sagging which is reduction in voltage through specified time range as illustrated in Figure 13. In this work, the three phase symmetrical voltage is sagging for about 3% from the nominal voltage. Without using STATCOM, when the inductive load is connected at PCC suddenly, it will absorb reactive power. The weak power grid cannot supply the required additional reactive power quickly and the DFIG output power is regulated to its optimum value.

As a result, the PCC voltage drops as illustrated in Figure 13. With using STATCOM at the PCC in this case, STATCOM responds rapidly by giving additional required reactive power. Therefore, the PCC voltage is regulated closely to its nominal voltage according to the reference desired value in AC voltage regulator with small overshoot shown in Figure 23. Also, the STATCOM has the ability to achieve DC voltage regulation of the DC-link as shown in Figure 24. Noting that the transmission line impedances at the side of DFIG and PCC are ($R_{T.L.} = 1\ m\Omega$ and $L_{T.L.} = 0.5\ mH$) and ($R_{T.L.} = 0.0229\ \Omega$ and $L_{T.L.} = 99\ \mu H$), respectively. The power grid impedance is ($R_G = 0.10472\ m\Omega$ and $L_G = 1\ \mu H$).

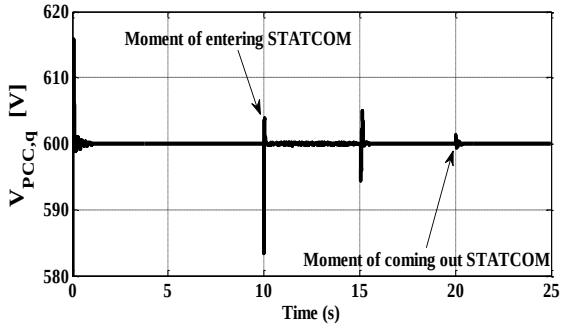

Fig. 23 The PCC voltage sag compensation at the DFIG wind turbine with STATCOM

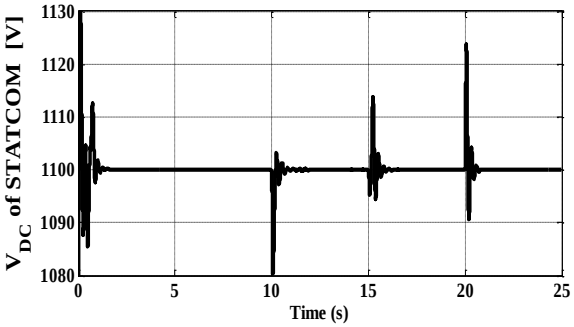

Fig. 24 The DC-link voltage of STATCOM during voltage sag compensation.

Secondly, the whole model is simulated under the same conditions mentioned above but in this case SAPF is used instead of STATCOM. As mentioned before the sudden inductive load is taken as a grid disturbance in the period from 10 seconds to 20 seconds during the same wind variation mentioned before. Before using SAPF, the PCC voltage is sagging for about 3% from the nominal voltage. With using SAPF at the PCC and the same effect of voltage sagging is created; in that case, SAPF will work with this disturbance based on load calculations using d-q axis reference frame as mentioned before. SAPF is controlled by hysteresis current controller to get switch control signals to inverter circuit. At the DC side of the inverter, the DC voltage is considered as a constant voltage (1100 V) and represented in MATLAB/Simulink by constant DC voltage source. SAPF will inject into PCC the required reactive power (supplying) based on inductive sudden load currents by SAPF actual currents.

As a result, the PCC voltage is regulated to be near from its nominal voltage in the period from 15 second to 20 second but in the period between 10 second to 15 second the voltage is raised up compared to the voltage in Figure 13 in the same period and not at its nominal voltage level because a small difference occurred when the wind speed is changed to 11 m/s. Figure 25a illustrates the PCC voltage before and after using SAPF. Figure 25b shows the PCC voltage for both SAPF and STATCOM after connection. It is absolutely clear that the STATCOM is

achieved better results than SAPF due to its AC voltage magnitude regulator. But SAPF depends on load calculations, the overall system of SAPF is affected by any change of the wind speed and it works according to this change of the wind speed according to its load calculations and hasn't the ability to restore the nominal voltage.

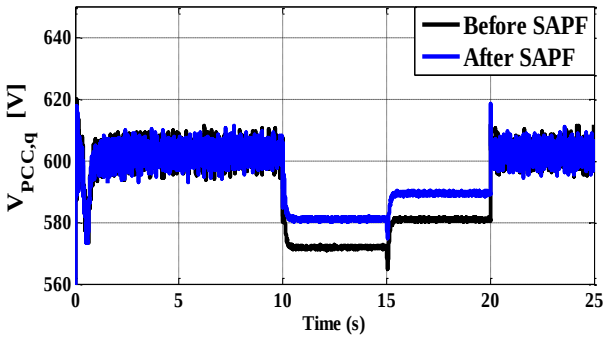

(a)

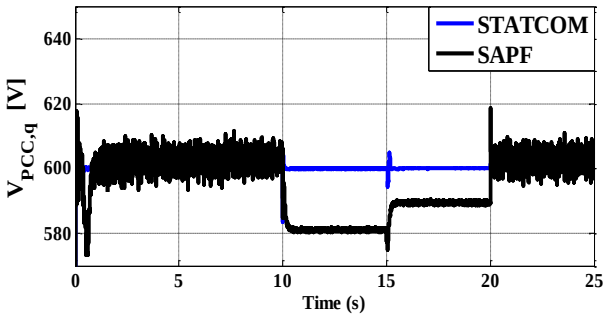

(b)

Fig. 25 The PCC voltage response
(a) Before and after SAPF connection, (b) After connection for both SAPF and STATCOM.

B. Comparison between STATCOM and SAPF connected at PCC under occurrence of three phase fault

The overall model is simulated in presence of three phase fault as a grid disturbance in the period from 10 seconds to 20 seconds during the same variation in wind speed mentioned before as shown in Figure 12a. The three phase fault block represents a three phase circuit breaker where the opening and closing times can be controlled from the simulation program. As a result of this the PCC voltage is sagging which is momentary decreasing in voltage over the time range without using STATCOM as illustrated in Figure 14.

The STATCOM is connected in shunt at PCC where the three phase fault occurred for variation in wind speed of DFIG. The overall model is simulated in presence of three phase fault as a grid disturbance in the period from 10 seconds to 20 seconds without using STATCOM as a result of this, the PCC voltage is sagging as illustrated in Figure 14. In this work, the three phase symmetrical voltage is sagging for about 4% from the nominal voltage. Where the weak power grid cannot supply required additional reactive power with quickly response and the DFIG output power is regulated to its optimum value. When the STATCOM with its capacitor ($C_m = 6.5\ mF$) is connected at the PCC in this case, STATCOM responds rapidly by supplying additional reactive power. As a result, the PCC voltage is regulated closely to its nominal voltage according to the reference desired value in AC voltage magnitude regulator with small overshoot shown in Figure 26.

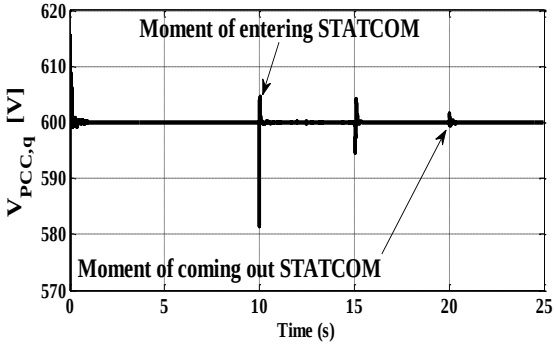

Fig. 26 The PCC voltage $v_{PCC,q}$ sag compensation at the DFIG wind turbine with STATCOM.

Also, the STATCOM has the ability to achieve DC voltage regulation of the DC-link as illustrated in Figure 27. Noting that, the transmission line impedances at the side of DFIG and PCC and power grid impedance are the same as case 1.

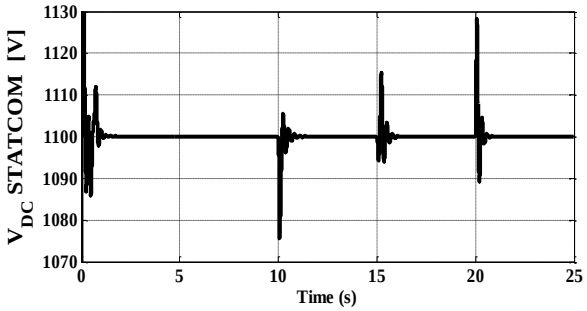

Fig. 27 The DC-link voltage of STATCOM during voltage sag compensation.

The same SAPF in previous case is used instead of STATCOM to inject into PCC the required reactive power (supplying) based on three phase fault currents by SAPF actual currents for the same conditions.

As a result, the PCC voltage is regulated to be closely to its nominal voltage in the period from 15 second to 20 second but in the period between 10 second to 15 second the voltage is raised up compared to the voltage in Figure 14 in the same period and not at its nominal voltage level because a small difference occurred when the wind speed is changed to 11 m/s. Figure 28a illustrates the PCC voltage before and after using SAPF. Figure 28b shows the PCC voltage for both SAPF and STATCOM after

connection. It is obviously clear that the STATCOM is achieved better results than SAPF due to its AC voltage magnitude regulator. But SAPF depends on fault current calculations, the overall system of SAPF is affected by any change of the wind speed and it works according to this change of the wind speed according to its fault current calculations and hasn't the ability to restore the nominal voltage.

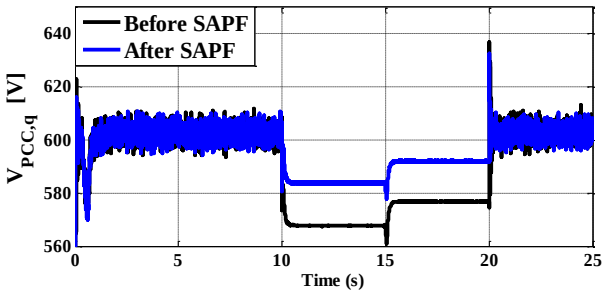

(a)

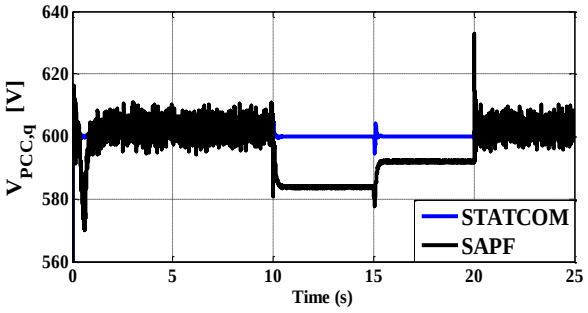

(b)

Fig. 28 The PCC voltage response
(a) Before and after SAPF connection, (b) After connection for both SAPF and STATCOM.

C. Comparison between STATCOM and SAPF connected at PCC under existence of sudden capacitive load

The overall model is simulated in presence of sudden capacitive load as a grid disturbance in the period from 10 seconds to 20 seconds without STATCOM. As a result of this the PCC voltage is swelling which is momentary increasing in voltage over the time range as shown in Figure 15. In this work, the three phase symmetrical voltage is swelling for about 2% from the nominal voltage. Before using the STATCOM, when the sudden capacitive load connected to PCC, it will supply reactive power into it. The weak power grid cannot absorb the required additional reactive power with rapidly response and the DFIG output power is regulated to its optimum value.

As a result, the PCC voltage increases as shown in Figure 15. When the STATCOM is connected at the PCC in this case, STATCOM responds rapidly by absorbing the additional reactive power. As a result, the PCC voltage is regulated nearly to its nominal voltage according to the reference desired value in AC voltage regulator with small overshoot shown in Figure 29. Also, the STATCOM has the ability to achieve DC voltage regulation of the DC-link as shown in Figure 30. Noting that the transmission line impedances at the side of DFIG and PCC are ($R_{T.L.} = 9\ m\Omega$ and $L_{T.L.} = 0.5\ mH$) and ($R_{T.L.} = 0.0179\Omega$ and $L_{T.L.} = 99\ \mu H$), respectively. The power grid impedance is ($R_G = 0.10472\ m\Omega$ and $L_G = 1\ \mu H$).

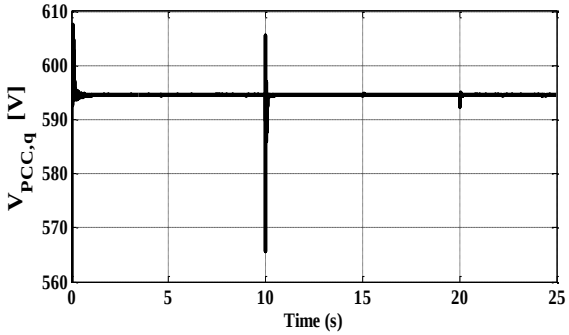

Fig. 29 The PCC voltage swell compensation at the DFIG wind turbine with STATCOM.

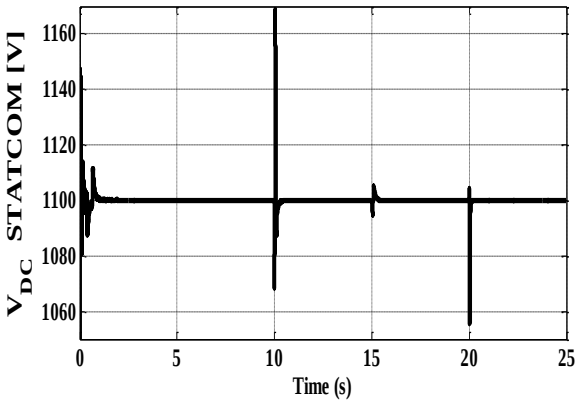

Fig. 30 The DC-link voltage of STATCOM during voltage swell compensation.

The same SAPF in case 1 is used instead of STATCOM in order to inject into PCC the required reactive power (absorbing) based on three phase sudden capacitive load currents by SAPF actual currents for the same conditions.

As a result, the PCC voltage is regulated to be near from its nominal voltage in the period from 15 second to 20 second but in the period between 10 second to 15 second the voltage is decreased compared to the voltage in Figure 15 in the same period and not at its nominal voltage level because a small difference happened when the wind speed is varied to 11 m/s.

Figure 31a illustrates the PCC voltage before and after using SAPF. Figure 31b shows the PCC voltage for both SAPF and STATCOM after connection. It is clearly that the STATCOM is achieved better results than SAPF due to its AC voltage magnitude regulator. But SAPF depends on sudden capacitive load calculations, the overall system of SAPF is affected by any change of the wind speed and it works according to this change of the wind speed

according to its load calculations and hasn't the ability to restore the nominal voltage.

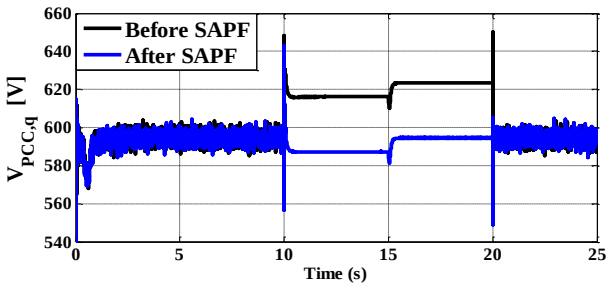

(a)

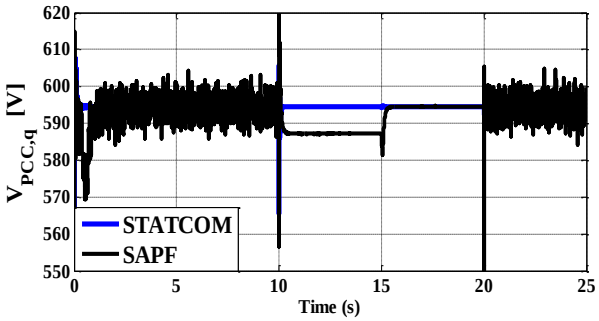

(b)

Fig. 31 The PCC voltage response
(a) Before and after SAPF connection, (b) After connection for both SAPF and STATCOM.

14. Conclusion

This work addressed a comparative analysis of two different control schemes for shunt devices installed in three phase distribution systems has been demonstrated. The performance of these control techniques has been analyzed for voltage swell and sag mitigations using time domain MATLAB/Simulink software. Under grid disturbances, the DFIG accomplished MPPT control technique. The proposed design of STATCOM under variation of wind speed in all cases achieved voltage regulation of DFIG wind turbine. In contrast, the suggested design of SAPF based on reactive power calculations of the load accomplished the voltage regulation of DFIG wind turbine around the nominal voltage. The simulation outcomes show that the proposed controller of STATCOM has the ability to regulate and enhance the PCC voltage response at DFIG wind turbine at its nominal voltage compared to SAPF based on its load calculations. STATCOM achieved better results than SAPF in regulation of the PCC voltage response at DFIG wind turbine due to its controller. Also, the results of both shunt devices give good performance and improve the system stability.

References

[1] Sompracha, C., Jayaweera, D., Tricoli, P. "*Particle swarm optimization technique to improve the energy efficiency of doubly-fed induction generators for wind turbines*", IET Renew. Power Gener., No. 18, pp.4890-4895, 2019.
https://doi.org/10.1049/joe.2018.9348

[2] Touzene, A., Yahyai, S.A., Melgani, F., "*Smart grid resources allocation using smart genetic heuristic*", IJCAT, Vol. 63, No. (1-2), pp.125-134, 2020.
https://doi.org/10.1504/IJCAT.2020.107918

[3] Slama, S., Errachdi, A., Benrejeb, M. "*Online MRAC method using neural networks based on variable learning rate for non-linear systems*", IJCAT, Vol. 60, No. 3, pp.215 – 224, 2019.
https://doi.org/10.1504/IJCAT.2019.100296

[4] Chien, T. H., Huang, Y. C. and Hsu, Y. Y. "*Neural Network-Based Supplementary Frequency Controller for a DFIG Wind Farm*", Energies, Vol. 13, No. 5320, pp.1-15, 2020.
https://doi.org/10.3390/en13205320

[5] Ahyaten, S. and Jalal El Bahaoui, J. "*Modeling of Wind Turbines Based on DFIG Generator*", Proceedings, Vol. 63, No. 16, pp.1-8, 2020.
https://doi.org/10.3390/proceedings2020063016

[6] Gomez, L. A. G., Grilo, A. P., Salles, M. B. C. and Filho, A. J. S. "*Combined Control of DFIG-Based Wind Turbine and Battery Energy Storage System for Frequency Response in Microgrids*", Energies, Vol. 13, No. 894, pp.1-17, 2020.
https://doi.org/10.3390/en13040894

[7] Kumar, V., Pandey, A. S. and Sinha, S. K. "*Stability Improvement of DFIG-Based Wind Farm Integrated Power System Using ANFIS Controlled STATCOM*", Energies, Vol. 13, No. 4707, pp.1-18, 2020.
https://doi.org/10.3390/en13184707

[8] Chauvin, M. A., Kavrakov B. S., Buele, J. and Aldás, J. V. "*Static Reactive Power Compensator Design, Based on Three-Phase Voltage Converter*", Energies, Vol. 14, No. 2198, pp.1-16, 2021.
https://doi.org/10.3390/en14082198

[9] Bialas, H., Pawelek, R. and Wasiak, I. "*A Simulation Model for Providing Analysis of Wind Farms Frequency and Voltage Regulation Services in an Electrical Power System*", Energies, Vol. 14, No. 2250, pp.1-17, 2021.
https://doi.org/10.3390/en14082250

[10] Almohaimeed, S. A. and Abdel-Akher, M. "*Power Quality Issues and Mitigation for Electric Grids with Wind Power Penetration*", Appl. Sci., Vol. 10, No. 8852, pp.1-24, 2020.
https://doi.org/10.3390/app10248852

[11] Ali, H.H., El Basuony, G.S. and Kamal, N.A. "*Maximum power production operation of doubly fed induction generator wind turbine using adaptive neural network and conventional controllers*", Int. J. Computer Applications in Technology, Vol. 65, No. 2, pp.173–187, 2021.
http://dx.doi.org/10.1504/IJCAT.2021.114984

[12] Ali, H.H., Kamal, N.A. and El Basuony, G.S. "*Two-Level Grid-Side Converter-Based STATCOM and*

Shunt Active Power Filter of Variable-Speed DFIG Wind Turbine-Based WECS Using SVM for Terminal Voltage", Int. J. of Service Science, Management, Engineering, and Technology, Vol. 12, No. 2, pp.169–202, 2021.
https://dx.doi.org/10.4018/ijssmet.2021030110

[13] Akanto, J. M., Hazari, Md. R. and Abdul Mannan, M. "*LVRT and Stability Enhancement of Grid-Tied Wind Farm Using DFIG-Based Wind Turbine*", Appl. Syst. Innov., Vol. 4, No. 33, pp.1-14, 2021.
https://doi.org/10.3390/asi4020033

[14] Alhato, M. M. and Bouallègue, S. "*Direct Power Control Optimization for Doubly Fed Induction Generator Based Wind Turbine Systems*", Math. Comput., Vol. 24, No. 77, pp.1-27, 2019.
https://doi.org/10.3390/mca24030077

[15] Kumar, N., Gaidhane, V.H., Mittal, R.K "*Cloud-based electricity consumption analysis using neural network*", IJCAT, Vol. 62, No. 1, pp.45 – 56, 2020.
https://doi.org/10.1504/IJCAT.2020.103917

[16] Shan, C. "*Computer-based outdoor sport sustainable development using wavelet neural network*", IJCAT, Vol. 61 No. 1/2, pp.112 – 117, 2019.
https://doi.org/10.1504/ijcat.2019.102108

[17] Sitharthan, R., Karthikeyan, M., Sundar, D.S., Rajasekaran, S. "*Adaptive hybrid intelligent MPPT controller to approximate effectual wind speed and optimal rotor speed of variable speed wind turbine*", ISA Transactions, Vol.96, pp.479-489, 2019.
https://doi.org/10.1016/j.isatra.2019.05.029

[18] Vaidyanathan, S., Pehlivan, I., Dolvis, L.G., Jacques, K., Alcin, M., Tuna, M., Koyuncu, I. "*A novel ANN-based four-dimensional two-disk hyperchaotic dynamical system, bifurcation analysis, circuit realisation and FPGA-based TRNG implementation*", IJCAT, Vol. 62, No. 1, pp.20 – 35, 2020.
https://doi.org/10.1504/IJCAT.2020.103921

[19] Zhong, L. P. "*A new topology and power control of grid-connected photovoltaic array*"", IJCAT, Vol. 61 No. 4, pp.287 – 291, 2019.
https://doi.org/10.1504/ijcat.2019.103292

[20] Qi Wang, Bin Wang, Wanwan Xu and Jiapan Xu . "*Research on STATCOM for reactive power flow control and voltage stability in microgrid*", 13th IEEE Conference on Industrial Electronics and Applications (ICIEA), 2018.
https://doi.org/10.1109/ICIEA.2018.8398126

[21] Priya Singh, S K Parida, Baru Chauhan and Niraj Choudhary. "*Online Voltage Stability Assessment Using Artificial Neural Network considering Voltage stability indices*", 21st National Power Systems Conference (NPSC), 2020.
https://doi.org/10.1109/NPSC49263.2020.9331954

[22] Zhou, Z., Liu, B., Wang, W., Wang, H. "*Research on grid-connected photovoltaic inverter based on quasi-PR controller adjusting by dynamic diagonal recurrent neural network*", IJCAT, Vol. 61, No. 3, pp.220 – 228, 2019.
https://doi.org/10.1504/ijcat.2019.102846

[23] Mohamed A. Ali. "*Hybrid technique for testing IEC 61850 based IEDs of distance protection*", Nineteenth International Middle East Power Systems Conference (MEPCON), 2017.
https://doi.org/10.1109/MEPCON.2017.8301205

[24] Sagar S. Patil, R. A. Metri and Omkar K. Shinde. "*Shunt active power filter for MV 12-pulse rectifier using PI with SMC controller*", International Conference on Circuit, Power and Computing Technologies (ICCPCT), 2017.
https://doi.org/10.1109/ICCPCT.2017.8074260

[25] Seyed Abbas Taher, Mohammad Hosein Alaee and Zahra Dehghani Arani . "*Model predictive control of PV-based shunt active power filter in single phase low voltage grid using conservative power theory*", 8th Power Electronics, Drive Systems & Technologies Conference (PEDSTC), 2017.
https://doi.org/10.1109/PEDSTC.2017.7910332

[26] Harsha Vanjani, U. K. Choudhury, Meha Sharma and Bhavesh Vanjani. "Takagi-sugeno *(TS)-type fuzzy logic controller for three-phase four-wire shunt active power filter for unbalanced load*", IEEE 7th Power India International Conference (PIICON), 2016.
https://doi.org/10.1109/POWERI.2016.8077227

[27] Azar, A.T., Serrano, F.E., Flores, M.A., Vaidyanathan, S., Zhu, Q. "*Adaptive neural-fuzzy and backstepping controller for port-Hamiltonian systems*", IJCAT, Vol. 62, No. 1, pp.1 – 12, 2020.
https://doi.org/10.1504/IJCAT.2020.103894